2D Space-Confined Synthesis of Few-Layer MoS_2 Anchored on Carbon Nanosheet for Lithium-Ion Battery Anode

Jingwen Zhou,[†,§] Jian Qin,[†,§] Xiang Zhang,[†] Chunsheng Shi,[†] Enzuo Liu,[†,‡] Jiajun Li,[†] Naiqin Zhao,[*,†,‡] and Chunnian He[*,†,‡]

[†]School of Materials Science and Engineering and Tianjin Key Laboratory of Composites and Functional Materials, Tianjin University, Tianjin, 300072, PR China and [‡]Collaborative Innovation Center of Chemical Science and Engineering, Tianjin 300072, PR China. [§]J.Z. and J.Q. contributed equally to this work.

ABSTRACT A facile and scalable 2D spatial confinement strategy is developed for *in situ* synthesizing highly crystalline MoS_2 nanosheets with few layers ($\leq$5 layers) anchored on 3D porous carbon nanosheet networks (3D FL-MoS_2@PCNNs) as lithium-ion battery anode. During the synthesis, 3D self-assembly of cubic NaCl particles is adopted to not only serve as a template to direct the growth of 3D porous carbon nanosheet networks, but also create a 2D-confined space to achieve the construction of few-layer MoS_2 nanosheets robustly lain on the surface of carbon nanosheet walls. In the resulting 3D architecture, the intimate contact between the surfaces of MoS_2 and carbon nanosheets can effectively avoid the aggregation and restacking of MoS_2 as well as remarkably enhance the structural integrity of the electrode, while the conductive matrix of 3D porous carbon nanosheet networks can ensure fast transport of both electrons and ions in the whole electrode. As a result, this unique 3D architecture manifests an outstanding long-life cycling capability at high rates, namely, a specific capacity as large as 709 mAh g^{-1} is delivered at 2 A g^{-1} and maintains ~95.2% even after 520 deep charge/discharge cycles. Apart from promising lithium-ion battery anode, this 3D FL-MoS_2@PCNN composite also has immense potential for applications in other areas such as supercapacitor, catalysis, and sensors.

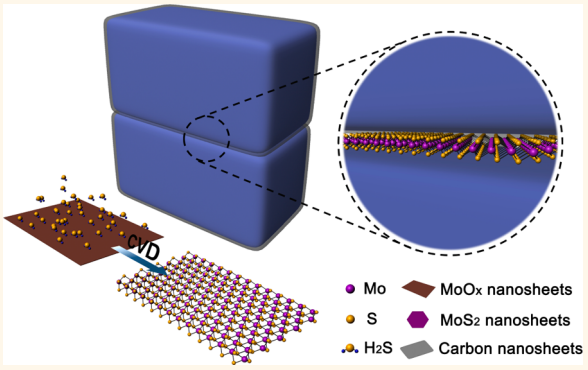

KEYWORDS: 2D space-confined synthesis · MoS_2 · carbon nanosheet · intimate interfacial contact · 3D network · lithium-ion battery anode

Lithium-ion batteries (LIBs), which possess the advantage of superior properties such as high energy and powder density, environmental benignity and long cycle life, are widely utilized in consumer electronics, transportation, and renewable energy storage devices. In particular, they are considered as a priority candidate of power sources for future hybrid electric vehicles and electric vehicles.[1,2] In order to further increase the energy density and power capability of current LIBs, enormous efforts have been made to develop high-performance electrode materials. In this regard, many metals, metal oxides or sulfides have been intensively explored as LIB anode materials in view of their large theoretical capacities, environmental friendliness and low-cost.[2−4]

As a representative two-dimensional (2D) layered transition metal sulfide,[3−7] molybdenum disulfide (MoS_2) nanosheet has attracted great scientific interest most recently for LIBs due to its 4-electron transfer reaction when hosting lithium ions, which enable its lithium storage capacity (669 mA h g^{-1}) much higher than that of the commercial graphite anode (372 mA h g^{-1}). Despite those predominant features, the practical application of MoS_2 as an anode material are yet to be realized thanks to its low intrinsic electric conductivity and large volume changes during the lithium insertion and extraction process, resulting in dramatic electrode pulverization and loss of electrical contact from the current collector, thus leading to poor cyclability and sluggish dynamic

* Address correspondence to cnhe08@tju.edu.cn, nqzhao@tju.edu.cn.

Received for review December 2, 2014 and accepted March 20, 2015.

Published online March 20, 2015
10.1021/nn506850e

of MoS_2 for lithium storage.[3,4,7] In order to overcome this obstacle, various strategies have been put forward to enhance the structural integrity and electrical conductivity of MoS_2-based anodes, such as synthesizing MoS_2 nanostructures with diverse morphologies[8−19] or coupling MoS_2 with electrically conductive polymer or carbon to construct nanocomposites.[7,20−52]

Up to now, a number of MoS_2/carbon composites have been exploited for LIB anodes, such as MoS_2 nanosheets embedded in porous carbon or carbon fibers,[21−23] carbon fibers or carbon spheres decorated with MoS_2 nanosheets,[24−30] MoS_2/carbon nanotubes composites,[31−35] and graphene supported MoS_2 nanosheets.[36−52] It has been reported that these carbon matrices can not only ameliorate the electric conductivity of the electrode greatly but also provide spaces to buffer the volume changes of MoS_2 during the charge/discharge process, thereby leading to enhanced cycling and rate performances.[21−52] Currently, the most frequently utilized approach for producing MoS_2/carbon composites is hydrothermal, or solution synthesis method, which involves the preparation of carbon matrix in advance and subsequent solution synthesis of MoS_2 decorated on the surface of the carbon matrix. Another method is to employ chemical vapor deposition (CVD) technique to *in situ* grow MoS_2 layers on a prefabricated carbon matrix. Unfortunately, most of these methods need complicated synthesis processes and thus are tedious, costly and time-consuming. Furthermore, the serious issue of quite low yield ranging from milligrams to grams would also highly hinder their large-scale application for commercial LIBs.[38,49]

On the other hand, when we investigated systematically the lithium storage performances of these MoS_2/carbon hybrids reported,[21−52] a phenomenon can be found: most of them can only endure less than 100 cycles at current densities in the range of 0.05−1 A g^{-1}, and long-life cycling capability at high rates that is highly crucial for the development of high-power LIBs has rarely achieved (see Table S1), which may be ascribed to the following factors. (i) 2D MoS_2 nanosheets are easy to reaggregate or restack because of their strong interlayer van der Waals attraction and large surface energy, which would greatly reduce the effective area of the electrode/electrolyte interface; (ii) the interfacial bonding between the MoS_2 materials and the carbon matrix is not very effective and intimate owing to the fact that in most cases the MoS_2 materials are just simply decorated on the surface of carbon matrix, which induces large interface resistance and severe structural instability; (iii) as stated above, most of the MoS_2 materials in these hybrids for LIB anodes were prepared by hydrothermal or solution synthesis method, in which the obtained low quality MoS_2 materials usually are amorphous or low-crystalline structures and have severe structural defects, thus leading to unsatisfactory structural stability and performance especially in the case of high-rate charge/discharge cycling.[23,26,30,32,34,44,47,50,52] Therefore, it is very urgent and desirable to develop a facile and scalable strategy for the fabrication of a novel MoS_2/carbon composite that can conquer the aggregation and restacking of MoS_2 and meanwhile has an intimate interfacial contact between MoS_2 and carbon matrix to enable overall structural integrity and excellent kinetics for storing lithium ions during the high-rate cycling process.

In this work, we demonstrated a novel 2D spatial confinement strategy to *in situ* fabricate MoS_2 nanosheets anchored on 3D porous carbon nanosheet networks (indicated with 3D FL-MoS_2@PCNNs), in which highly crystalline MoS_2 nanosheets with few layers ($\leq$5 layers) very homogeneously and tightly lie on the surface of carbon nanosheet walls (with thickness $\leq$3 nm). In this straightforward one-step solid-phase synthesis strategy, 3D self-assembly of cubic NaCl particles is adopted to not only serve as a template to direct the growth of 3D porous carbon nanosheet networks,[53] but also create a 2D-confined space to achieve the construction of few-layer MoS_2 nanosheets robustly lain on carbon nanosheet walls, which offer several advantages as LIB anodes: First of all, few-layer MoS_2 nanosheets with ultrathin nature and high quality can provide a short length for the steady transport of both electrons and ions. Second, the intimate surface-to-surface contact between MoS_2 and carbon nanosheets not only can effectively restrain the aggregation of MoS_2 nanosheets and buffer their volume expansion and thus maintain structural integrity of the electrode, but also enable fast electron and ion transportation across the interface between MoS_2 and carbon nanosheets.[54] Finally, the 3D carbon nanosheet networks with porous nature, large surface area and excellent electrical conductivity can facilitate three-dimensional diffusion and transport of electrons and ions in the whole electrode and further offer ample void space for buffering the volume expansion of MoS_2 during discharge (lithiation).[53] With these inspiring merits, this novel 3D architecture demonstrates an outstanding long-life cycling capability at high rates; *i.e.*, a specific capacity as large as 709 mAh g^{-1} is delivered at 2 A g^{-1} and maintains ~95.2% even after 520 deep charge/discharge cycles. Moreover, this one-step synthesis approach accomplished in the solid-phase state may be very suitable for scalable and low-cost industrial production of MoS_2/carbon composites.

RESULTS AND DISCUSSION

The fabrication of 3D FL-MoS_2@PCNNs is schematically depicted in Figure 1. The first step of the synthesis process consists in dissolving NaCl, $C_6H_8O_7$, NH_2CSNH_2, and $(NH_4)_6Mo_7O_{24}\cdot 4H_2O$ in distilled water to obtain an even solution. In the second step, the water in the

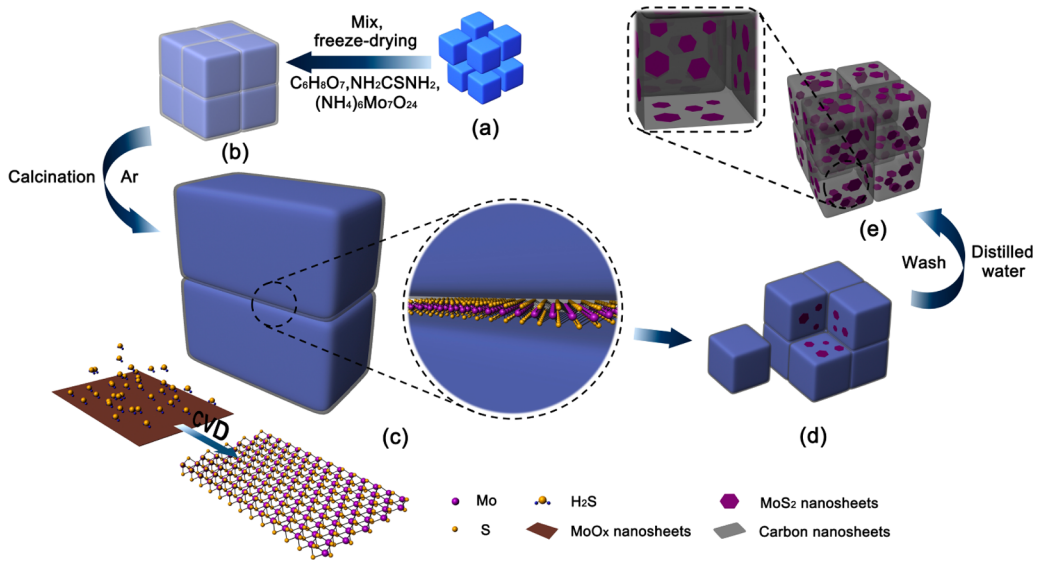

Figure 1. Schematics depicting the fabrication procedure of 3D FL-MoS_2@PCNNs: (a) NaCl particles, (b) 3D NaCl self-assembly coated with $NH_2CSNH_2-(NH_4)_6Mo_7O_{24}-C_6H_8O_7$, (c) illustration of the growth of MoS_2 nanosheets within the 2D-confined space between the NaCl surfaces, (d) 3D NaCl covered with FL-MoS_2@CNNs, and (e) 3D FL-MoS_2@PCNNs.

resulting solution is removed using a freeze-drying technology, which ensures the preservation of the uniform dispersion of NaCl, $C_6H_8O_7$, NH_2CSNH_2, and $(NH_4)_6Mo_7O_{24}\cdot 4H_2O$ in the precursor gel. Moreover, thanks to the cubic crystal structure of NaCl, this step can also guarantee that the NaCl particles uniformly coated with an ultrathin $NH_2CSNH_2-(NH_4)_6Mo_7O_{24}-C_6H_8O_7$ complex film are self-assembled into 3D framework (Figure 1b).[53] In the third step, 3D complex of $NH_2CSNH_2-(NH_4)_6Mo_7O_{24}-C_6H_8O_7$/NaCl is heated at 750 °C under Ar. During the heat-treatment process, the $(NH_4)_6Mo_7O_{24}$ is decomposed to ultrathin MoO_x nanosheets within the 2D-confined space between the NaCl surfaces, and NH_2CSNH_2 is hydrolyzed to H_2S, and then MoO_x nanosheets react with H_2S to *in situ* form 2D ultrathin MoS_2 nanosheets (Figure 1c). Meanwhile, the citric acid is carbonized within the 2D-confined space to form ultrathin carbon nanosheet that tightly pins the MoS_2 nanosheets on its surface (Figure 1d). Finally, the NaCl particles in the as-made products were easily eliminated with deionized water to obtain pure 3D FL-MoS_2@PCNNs (Figure 1e). Importantly, it should be pointed out that above heat-treatment process is implemented by the solid-phase complex, which makes this one-step *in situ* synthesis approach very easily controllable, low-cost, and very suitable for scalable industrial production of MoS_2/carbon composites. Moreover, this one-step solid-phase fabrication process can avoid post tedious separation and purification procedures as well as agglomerations of MoS_2 nanosheets, but these issues are almost inevitable for the liquid phase synthesis method.[53]

Figure 2a shows the X-ray diffraction (XRD) pattern of the as-made 3D FL-MoS_2@PCNNs. Besides the weak and broadened diffraction peak at 25−28° assigned to the phase of carbon materials, all sharp diffraction peaks agree well with the hexagonal MoS_2 planes (JCPDS card No. 37−1492), implying the high crystalline and phase purity of MoS_2 materials in the 3D FL-MoS_2@PCNNs. It is noteworthy that the strong peak at 14.2°, which is due to the (002) plane of MoS_2, indicates the ordered stacking of S−Mo−S layers.[37] According to thermogravimetric analysis (TGA, Supporting Information Figure S1), the MoS_2 content in the product can be calculated to be approximately 67.1 wt %, which is comparable to previously reported MoS_2/carbon composites.[24−26,38−43]

Figure 2b and Figure S2a exhibit scanning electron microscopy (SEM) images of the product (3D FL-MoS_2@PCNNs). As can be seen, the sample possesses a highly interconnected 3D porous network with submicrometer-sized macropores and the outer edges of the network walls demonstrate the low contrast and obvious corrugations, revealing that the walls with ultrathin thickness (≤3 nm) should have excellent mechanical flexibility.[53] In order to explore the microstructures of the 3D FL-MoS_2@PCNNs, transmission electron microscopy (TEM), high-resolution TEM (HRTEM), scanning transmission electron microscopy (STEM) and elemental mapping were performed. According to Figure 2c, we can further ascertain an interconnected 3D porous network, well consistent with above SEM analysis. When examined the TEM images in detail, it is clearly discerned that a large number of uniform hexagonal or quasi-hexagonal MoS_2 nanosheets with a lateral size ranging from 50 to 300 nm and a large aspect ratio homogeneously lie on the surface of carbon nanosheet walls (as shown in Figure 2c,d), thus achieving a surface to surface contact (Figure 2e).[54] STEM image (Figure S2b) and the C, Mo and S element mappings

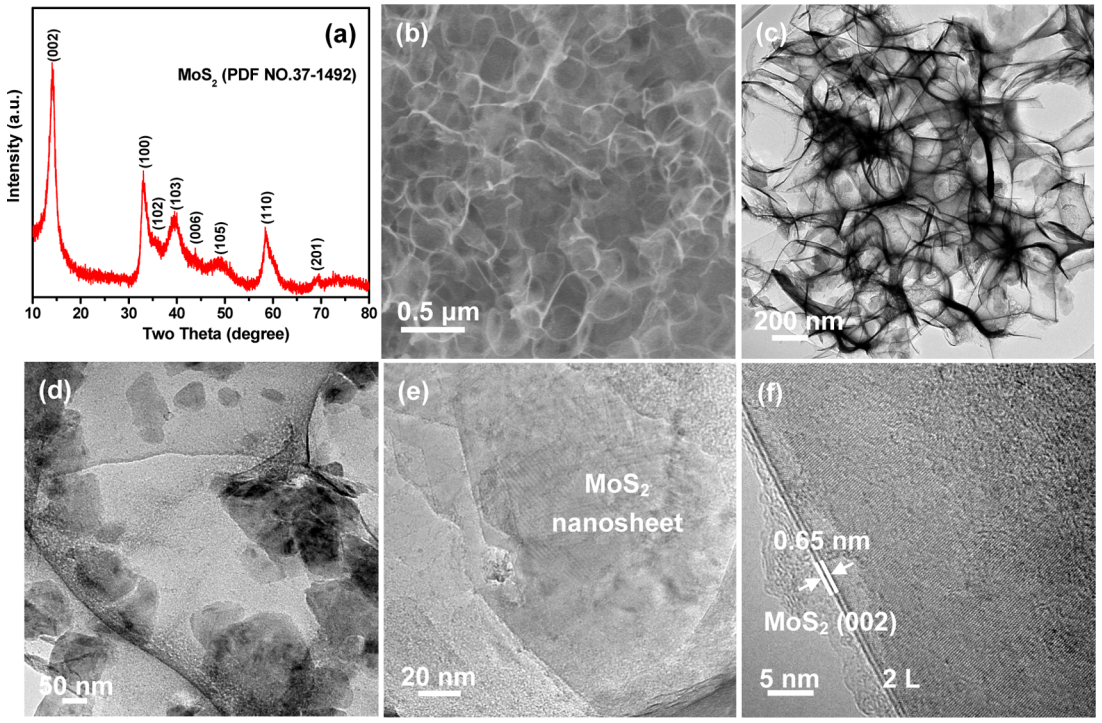

Figure 2. (a) XRD pattern, (b) SEM and (c−f) TEM images of 3D FL-MoS_2@PCNNs.

(Figure S2c−f) of the as-formed 3D FL-MoS_2@PCNNs further give the proof of the even distribution of MoS_2 nanosheets in the 3D carbon network. More importantly, it is worth noting that, during the preparation process of TEM sample, even after a vigorous sonication for more than 48 h, the MoS_2 nanosheets are still firmly pinned on the carbon nanosheets with robust surface-to-surface contact (see Figure S2g,h), suggesting the strong and effective interfacial bonding between MoS_2 and carbon nanosheets. It is believed that such intimate surface-to-surface contact between MoS_2 and carbon nanosheets not only can effectively hamper the aggregation and restacking of MoS_2 nanosheets for ensuring the whole structural integrity and good cycling stability, but also markedly facilitates fast and stable electron and ion transport across the interface for improving the rate capacity and cyclability.[54−58]

Furthermore, the thickness (layer number) and crystallinity of the MoS_2 and carbon nanosheets were determined using HRTEM in details. From HRTEM images of Figure 2f and Figure 3a, we can observe that all of the MoS_2 nanosheets are highly crystallized and composed of monolayer, bilayer or a few layers only (≤5 layers). HRTEM image of Figure 3b taken from a typical MoS_2 nanosheet further reveals that the atoms exhibit obvious hexagonal atomic arrangement with the spacing of the adjacent lattice being 0.27 and 0.16 nm, which are in good accordance with typical (100) and (110) planes of the pristine 2H-MoS_2, respectively.[59−62] Figure 3c shows the reciprocal space image obtained by Fourier transform of Figure 3b, further demonstrating distinct hexagonal crystal structure of MoS_2. Figure S2i displays the EDS spectrum of the bilayer MoS_2 nanosheet, which validates that this nanosheet possesses both sulfur and molybdenum. With regard to the carbon nanosheet walls, HRTEM images of Figure 3d,e reveal that they have good crystallization and their thickness is generally 3 nm or less than 3 nm. In addition, it is also found that the thickness of MoS_2 and carbon nanosheets, or the content of MoS_2 in the 3D networks can be tuned by adjusting the preparation conditions, such as the content of NaCl, and the ratio of MoS_2 precursor to carbon precursor. With a larger content of NaCl and higher ratio of MoS_2 precursor to carbon precursor, thinner carbon nanosheet walls and MoS_2 nanosheets with larger content can be synthesized in the 3D composites.[53]

In order to unveil the growth mechanism of 3D FL-MoS_2@PCNNs, a series of designed experiments were performed. First, when the mixture (NH_2CSNH_2−$(NH_4)_6Mo_7O_{24}$−$C_6H_8O_7$) without adding NaCl was treated under the same condition as that for the preparation of 3D FL-MoS_2@PCNNs, we found that the as-obtained product is just micrometer-sized carbon blocks embedded with disordered MoS_2 (indicated with MoS_2/C composite) and there is no porous carbon networks and MoS_2 nanosheets (see Figure S3). This remarkable morphological difference highlights the crucial role of NaCl in the growth of 3D FL-MoS_2@PCNNs. To verify this, the precursor gel of NH_2CSNH_2−$(NH_4)_6Mo_7O_{24}$−$C_6H_8O_7$/NaCl after freeze-drying dehydration, the heat-treatment products before removing NaCl and the heat-treatment products of $C_6H_8O_7$/NaCl without NH_2CSNH_2−$(NH_4)_6Mo_7O_{24}$ were characterized by SEM. From the SEM image of

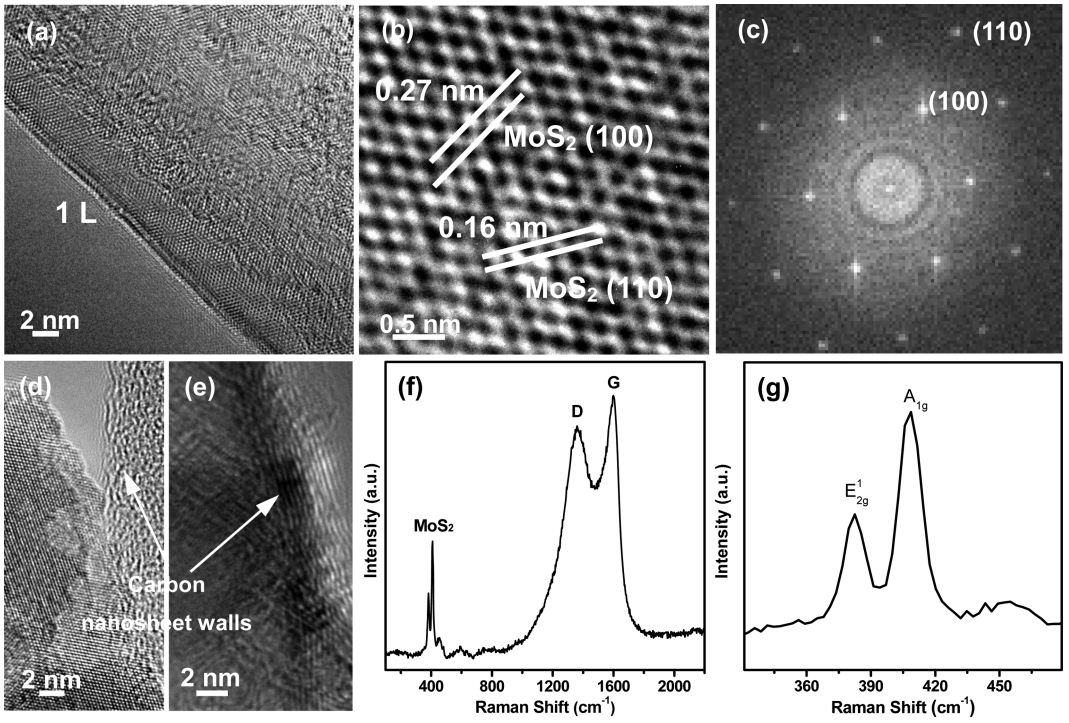

Figure 3. (a,b) HRTEM images of typical MoS_2 nanosheets. (c) Fourier-transformed electron diffraction of (b). (d,e) HRTEM images of typical carbon nanosheet walls. (f) Raman spectrum of 3D FL-MoS_2@PCNNs. (g) Magnified Raman spectrum of 3D FL-MoS_2@PCNNs, exhibiting the typical MoS_2 characteristic signature.

Figure S4a, it can be distinctly seen that the cubic particles, which are NaCl evenly coated with an ultrathin film of NH_2CSNH_2−$(NH_4)_6Mo_7O_{24}$−$C_6H_8O_7$, were self-assembled into 3D architecture during the freeze-drying process. After heat-treatment, this 3D structure was still maintained and in fact the FL-MoS_2@CNNs were synthesized along the surface of NaCl self-assembly (Figure S4b).[53] As for the heat-treatment products of $C_6H_8O_7$/NaCl without adding NH_2CSNH_2−$(NH_4)_6Mo_7O_{24}$, it can be observed that a 3D porous carbon nanosheet network (indicated with 3D PCNNs) that perfectly replicates the template of 3D NaCl self-assembly were obtained (Figure S4c−f). According to above results, we affirmatively deduced that the 3D NaCl self-assembly builds a 2D confined void between the NaCl surfaces that spatially directs the formation of 2D MoS_2 nanosheets and 2D citric acid-derived carbon nanosheets. In addition, we have also employed XRD and SEM analyses to investigate the composition and microstructure of the products obtained by calcining the mixture ($(NH_4)_6Mo_7O_{24}$/NaCl) without $C_6H_8O_7$ and NH_2CSNH_2 and its reaction products with H_2S, as well as the products obtained by heat-treating the single material of $(NH_4)_6Mo_7O_{24}$ and its reaction products with H_2S. It can be discerned that at low temperature, MO_x nanosheets were obtained when calcining the $(NH_4)_6Mo_7O_{24}$ in the presence of NaCl (Figure S5a,c,d,g). As these MO_x nanosheets further reacted with H_2S, MoS_2 nanosheets were synthesized (Figure S5b,g). In regard to the calcining products of single $(NH_4)_6Mo_7O_{24}$, a mass of bulk MO_x materials can be observed (Figure S5e). After further reaction with H_2S, these bulk MO_x materials can be converted to bulk MoS_2 materials (Figure S5f,h). On the basis of the above evidence and previous works,[42,58−60] we considered that the formation process of our 3D FL-MoS_2@PCNNs may be as follows. At relatively low temperatures, the $(NH_4)_6Mo_7O_{24}$ is decomposed to ultrathin MoO_x nanosheets within the 2D-confined space between the NaCl surfaces and the NH_2CSNH_2 is hydrolyzed to H_2S, CO_2 and NH_3. The detailed reaction equations are described as follows.[41,42]

$$3(NH_4)_6Mo_7O_{24}\cdot 4H_2O \rightarrow (14x - 24)NH_3 + (21 - 7x)N_2 + 21MoO_x + (84 - 21x)H_2O \quad (1)$$

$$NH_2CSNH_2 + 2H_2O \rightarrow 2NH_3 + H_2S + CO_2 \quad (2)$$

At higher temperatures, ultrathin MoO_x nanosheets react with H_2S to form few-layer MoS_2 nanosheets, and the reaction can be expressed as follows.[41,42,58,59]

$$4MoO_x + (x+6)H_2S \rightarrow 4MoS_2 + (x-2)SO_3 + (x+6)H_2O \quad (3)$$

Meanwhile, citric acid is carbonized within the 2D-confined space to generate ultrathin carbon nanosheet[53] that tightly anchor the MoS_2 nanosheets on its surface, leading to the remarkably enhanced interfacial contact between the MoS_2 nanosheets and carbon matrix. Ultimately, the NaCl particles in the as-synthesized products were easily removed by deionized water, and then pure 3D FL-MoS_2@PCNNs

were obtained. However, the validation for the detailed formation process of 3D FL-MoS_2@PCNNs should require more careful investigations, and in depth systematic study is needed in the future.

3D FL-MoS_2@PCNNs were further evaluated by Raman spectroscopy to confirm the carbon material and MoS_2 structure, with the results illustrated in Figure 3f. It can be obviously revealed that the spectrum exhibits two characteristic peaks of carbon materials, located at 1361 and 1601 cm^{-1} and corresponding to the D and G bands, respectively. It is well-known that the D band is ascribed to the vibrations of carbon atoms with dangling bonds for the in-plane terminations of disordered graphite, while the G band is the result of the E_{2g} mode (stretching vibrations) in the basal plane of the crystalline graphite.[63] As shown in Figure 3f, the Raman intensity of the G band is higher than the D band, indicating that the carbon materials in the 3D networks are mainly composed of well-crystallized graphite, in good agreement with TEM results above. In addition to the typical peaks for carbon materials, the other two distinct peaks around at the bands of 408 and 382 cm^{-1} are MoS_2 characteristic signature and associated with out-of-plane A_{1g} (out-of-plane symmetric displacements of S atoms along the *c*-axis) and in-plane E^1_{2g} (the in-plane displacement of Mo and S atoms) Raman mode, respectively (Figure 3g).[59−62] X-ray photoelectron spectroscopy (XPS) analysis was carried out to further clarify the chemical composition of Mo and S in the 3D FL-MoS_2@PCNNs. As seen in Figure S6a, there are two characteristic peaks at 229.5 and 232.7 eV, which correspond to the Mo $3d_{5/2}$ and Mo $3d_{3/2}$ orbitals, respectively, suggesting a Mo (IV) characteristic in MoS_2. The binding energies located at 162.3 and 163.5 eV are due to S $2p_{3/2}$ and $2p_{1/2}$, respectively (Figure S6b). Above binding energies are all in good agreement with values of MoS_2 crystal reported previously.[59−62] Detailed compositional analysis from XPS indicates that the atomic ratio of Mo and S is about 1:2, further giving the evidence of the synthesis of MoS_2 in the product.

Nitrogen adsorption−desorption measurements were utilized to study the texture and porous nature of the 3D FL-MoS_2@PCNNs. As exhibited in Figure S7a, their adsorption−desorption isotherms coincide with a type IV isotherm. The specific surface area is calculated to be 355 $m^2\ g^{-1}$ by the Brunauer−Emmett−Teller (BET) analysis, which is much larger than the MoS_2/C composite (3.93 $m^2\ g^{-1}$, see Figure S7c) and the bulk MoS_2 powders (23 $m^2\ g^{-1}$). The pore size distribution derived from the Barrett−Joyner−Halenda (BJH) method is depicted in Figure S7b. Besides the macropores unveiled from the SEM and TEM images, it can be disclosed that the 3D architecture has a broad pore size distribution that includes a mass of micro- (0.5−2 nm) and mesopores (2−36 nm). Obviously, the macropores are generated by the soluble template of NaCl particles. As for the micropores and mesopores in the 3D architecture, they may be related to the porous structure and defects inside the carbon nanosheets as a result of releasing gas during the high-temperature heat-treatment process.[53] In order to clarify the origin of the high surface area of 3D FL-MoS_2@PCNNs, we have also investigated the porous nature of 3D PCNNs produced by calcining the mixture ($C_6H_8O_7$/NaCl) without adding NH_2CSNH_2−$(NH_4)_6Mo_7O_{24}$. As can be seen in Figure S8, the 3D PCNNs possess a very high surface area of 1090 $m^2\ g^{-1}$ together with hierarchical porous structure from micropores to macropores. On the basis of the above analysis, it can be speculated that the high surface area of 3D FL-MoS_2@PCNNs should be attributed to the joint action between the porous carbon network with very high surface area and the ultrathin MoS_2 nanosheets with low surface area. The unique hierarchical porous structure combined with high specific surface area of 3D FL-MoS_2@PCNNs can facilitate the mass transport of electrolytes into the active materials and the fast diffusion of lithium ions in the whole electrode during lithium storage, and also can provide ample void space to release the mechanical strain of the active material without leading to pulverization during lithium insertion/extraction, which are highly desirable features for energy storage application or other applications.[38,53,61]

The electrochemical properties of MoS_2 nanosheets and 3D FL-MoS_2@PCNNs were first evaluated by cyclic voltammogram (CV). Figure S9a displays the CV curves for the fist three cycles of the MoS_2 nanosheet electrode at a sweep rate of 0.1 mV s^{-1} within a potential window of 0.005−3.0 V (*vs* Li^+/Li). Similar to MoS_2 anodes reported previously,[9,11,38] two dominant reduction peaks at 1.09 and 0.50 V appear only in the first cycle, which are commonly ascribed to insertion of lithium ions into the interlayer space of MoS_2 to form Li_xMoS_2, and the reduction of Li_xMoS_2 to Li_2S and metallic Mo nanoparticles *via* a conversion reaction, respectively. As for the oxidation peak at around 2.33 V, which is due to the oxidation of Li_2S to S and lithium ions, it becomes much weaker and has a right shift after the first cycle, indicating that these MoS_2 nanosheets might have poor structural stability and cycling performance,[9,11,38] as further revealed in the following electrochemical tests. In the subsequent cycles, three new reduction peaks at around 1.93, 1.10, and 0.27 V emerge that are attributed to the three reactions expressed in the following eqs 4−6.[36,49]

$$2Li^+ + S + 2e^- \rightarrow Li_2S \quad (4)$$

$$MoS_2 + xLi^+ + xe^- \rightarrow Li_xMoS_2 \quad (5)$$

$$Li_xMoS_2 + (4 - x)Li^+ + (4 - x)e^- \rightarrow Mo + 2Li_2S \quad (6)$$

With regard to the 3D FL-MoS_2@PCNN electrode (Figure 4a), most of the reduction and oxidation peaks in its CV curves are weaker as well as exhibit a slight

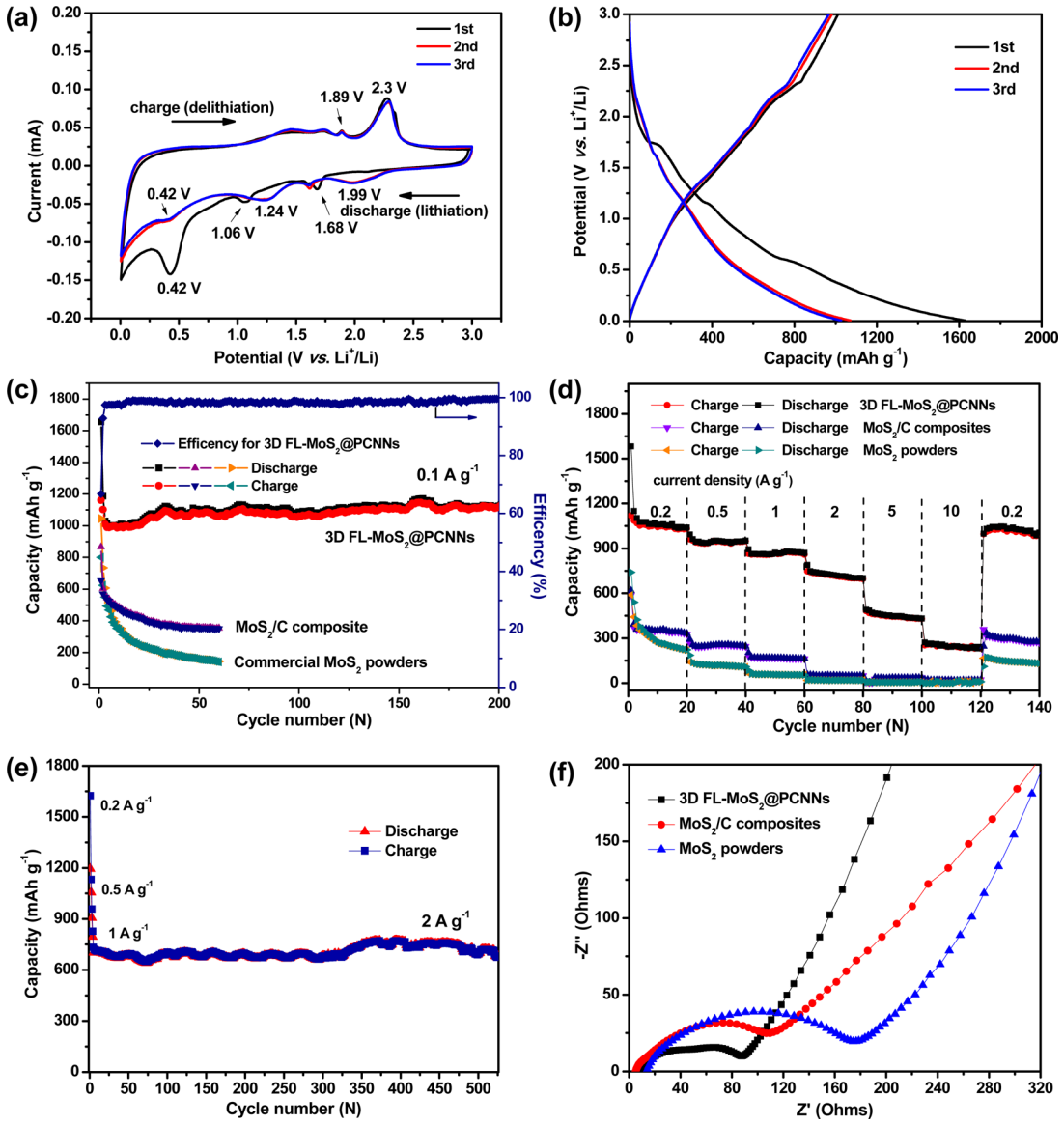

Figure 4. (a) CVs of the 3D FL-MoS_2@PCNN electrode at a scanning rate of 0.1 mV s^{-1} during the initial three cycles. (b) Galvanostatic discharge/charge profiles of the 3D FL-MoS_2@PCNN electrode at 0.1 A g^{-1}. (c) Cycle behaviors and (d) Rate-capability performance of the electrodes of 3D FL-MoS_2@PCNNs, MoS_2/C composites and commercial MoS_2 powders. (e) Capacity retention of the 3D FL-MoS_2@PCNN electrode at current densities of 0.2, 0.5, and 1 A g^{-1} for initial fix cycles and then 2 A g^{-1} for subsequent 520 cycles. (f) Nyquist plots of the AC impedance spectra for the electrodes of 3D FL-MoS_2@PCNNs, MoS_2/C composites, and commercial MoS_2 powders after the rate capability test.

shift compared with the CV curves of MoS_2 nanosheet electrode, which may be induced by the combined effects of both ultrathin MoS_2 nanosheets (Figure S9a) and 3D PCNNs (Figure S9b) electrochemically reacted with lithium ions.[24,36,38,49] The new weak oxidation peak at about 1.89 V and reduction peak at about 1.68 V, which are absent in the CV curves of MoS_2 nanosheet electrode (Figure S9a), should be ascribed to the reversible lithium storage on 3D PCNNs, further indicating both the 3D PCNNs and MoS_2 nanosheets in the 3D architecture have the ability to store lithium ions during the electrochemical process.[24,36,38,49] In addition, it can be noted that after the first cycle the subsequent CV curves of 3D FL-MoS_2@PCNN electrode almost overlap, indicating the excellent retention of structural stability for the 3D architecture during the charge/discharge process.[53]

Figure S9c and Figure 4b present the galvanostatic charge−discharge voltage profiles of the MoS_2 nanosheet and 3D FL-MoS_2@PCNN electrode, respectively, for the first, second, and third cycles at a constant current density of 0.1 A g^{-1}. In the first discharge voltage profile of the MoS_2 nanosheet electrode (Figure S9c), two distinct voltage plateaus at around 1.2 and 0.7 V can be observed. According to previous reports,[9,11,38] the plateau at ~1.2 V should be assigned to lithium insertion into the interlayer space of MoS_2 to form Li_xMoS_2, while the plateau at ~0.7 V is ascribed to

the decomposition of Li_xMoS_2 to Li_2S and Mo through a conversion reaction process. After the first discharge cycle, there appear three new inapparent plateaus at around 1.8, 1.0, and 0.3 V, which are in good accordance with MoS_2 anodes reported previously.[36,49] In the charge profile for the MoS_2 nanosheet electrode, a plateau at around 2.3 V is due to the oxidation of Li_2S into S and lithium ions.[9,11,38] Therefore, above voltage plateaus in the charge/discharge profiles are well consistent with the reduction and oxidation peaks in the CV curves of the MoS_2 nanosheet electrode. As to the charge/discharge voltage profiles (Figure 4b) of the 3D FL-MoS_2@PCNN electrode, it can be found that all voltage plateaus are not very apparent in comparison with MoS_2 nanosheet electrode, in good agreement with that from the above CV curves (Figure 4a). This result should be caused by the combined effects of MoS_2 nanosheet (Figure S9c) and 3D PCNNs (Figure S9d) and further validates that both the MoS_2 nanosheet and 3D PCNNs are the active materials for electrochemically hosting lithium ions.[24,36,38,49] In the first cycle of 3D FL-MoS_2@PCNN electrode, its initial discharge and charge specific capacities are approximately 1654 and 1161 mAh g^{-1}, respectively, showing a Coulombic efficiency (CE) of ~70% (in contrast, the 3D PCNN electrode exhibits a much lower CE of 46%, as shown in Figure S9d). The initial irreversible capacity loss of the FL-MoS_2@PCNN electrode might be due to the inevitable formation of solid electrolyte interphase (SEI) and decomposition of electrolyte.[7,21,42]

Figure 4c and Figure S10 exhibit the galvanostatic cycle behaviors of 3D FL-MoS_2@PCNNs, MoS_2/C composite, commercial MoS_2 powder, MoS_2 nanosheet and 3D PCNNCs at a current density of 0.1 A g^{-1}, together with the Coulombic efficiency of FL-MoS_2@PCNN electrode depicted in Figure 4c. For the 3D FL-MoS_2@PCNNs, the reversible specific capacities of ~1128 and ~1127 mAh g^{-1} were delivered at the second cycle and after 200 cycles, respectively, leading to a capacity retention of nearly 100% after 200 charge/discharge cycles. Although their initial Coulombic efficiency is only ~70% in the first cycle, it rapidly increases to ~97% in the third cycles and retains above 99% after 14th cycles, suggesting efficient electron and ion transport and facile lithium ion insertion and extraction in the FL-MoS_2@PCNN electrode.[53] In contrast, the MoS_2/C composite, MoS_2 nanosheets, and MoS_2 powders show continuous and progressive capacity decay along with cycling processes at the same current density. After 50 cycles, MoS_2/C composite, MoS_2 powder, and MoS_2 nanosheet electrodes can only deliver 354, 157, and 223 mAh g^{-1}, respectively. As for the 3D PCNNC electrode, it shows good cycling stability, but only has a low capacity of bout 345 mAh g^{-1} after 50 cycles. The low capacities of either of the single MoS_2 nanosheet or 3D PCNNC electrode indicate that the MoS_2 nanosheets and 3D PCNNCs should have a favorable synergistic effect that contributes to the much better reversible capacity and cycling performance of 3D FL-MoS_2@PCNNs.[24]

Furthermore, Figure 4d demonstrates the much improved rate capability for the 3D FL-MoS_2@PCNN electrode. As the current rates increase from 0.2 to 0.5, 1, 2, 5, and 10 C (1 C = 1 A g^{-1}), the 3D FL-MoS_2@PCNNs display reversible and stable capacities of 1060, 950, 880, 710, 480, and 250 mA h g^{-1}, respectively. Notably, these values are much higher than those of MoS_2/C composite and MoS_2 powders. Importantly, when the current density decreases to 0.2 A g^{-1} after cycling under high current densities, 3D FL-MoS_2@PCNNs can still regain a reversible capacity near 1050 mA h g^{-1} compared with the 1075 mAh g^{-1} obtained in the initial cycle at 0.2 C rate, resulting in a capacity fading of only 2%. Inspired by the good cycling and rate performance, the long-term cyclability evaluation of the 3D FL-MoS_2@PCNN electrode was also carried out at a high rate of 2 C (2 A g^{-1}), with the evolution of the specific capacity displayed in Figure 4d. Very strikingly, a specific capacity as high as 709 mAh g^{-1} was delivered at 2 A g^{-1} and maintains ~95.2% (676 mAh g^{-1}) even after 520 deep charge/discharge cycles, with a capacity-decay rate of only 0.009% per cycle. Such excellent long-life cycling capability at high rates of our 3D FL-MoS_2@PCNN electrode are superior to previous MoS_2 nanostructures,[8−19] and MoS_2/carbon composites[7,20−52] (as shown in Table S1). To our best knowledge, very few previous MoS_2-based anodes have reported to be able to endure hundreds of cycles at high rates. For example, Xu *et al.* constructed MoS_2 nanosheets-decorated CMK-3 by a hydrothermal process; the designed MoS_2/CMK-3 anode delivered a discharge capacity of 934 mAh g^{-1} after 150 cycles at a current density of 0.4 A g^{-1}.[21] Very recently, MoS_2 sheets-decorated carbon nanofibers also produced by the hydrothermal method were developed as a LIB anode with 300 cycles, which exhibited a capacity of 688 mAh g^{-1} at 1 A g^{-1} after about 300 cycles, with a capacity retention of about 76.4%[24] In comparison with these prominent results, the 3D FL-MoS_2@PCNN electrode in this work demonstrates even more superior long-life high-rate cycling capability, which delivers ~709 mAh g^{-1} at a higher current density of 2 A g^{-1} for over 500 cycles while exhibiting a capacity retention as high as 95.2%.

The electrochemical impedance spectra measurements on the electrodes of 3D FL-MoS_2@PCNNs, MoS_2/C composites and commercial MoS_2 powders before cycling and after the rate capability test were also conducted to gain deeper insights into the remarkable enhanced electrochemical reaction kinetics of 3D FL-MoS_2@PCNNs. Figure S11a and Figure 4f shows the Nyquist plots of the AC-impedance spectra obtained for the three samples before cycling and after the rate capability test, respectively. In accordance with the

impedance spectra of other MoS_2-based anodes,[7,21,42] these impedance spectra are all composed of a medium-to-high frequency depressed semicircle and a low-frequency sloping straight line. The high frequency semicircle is an indication of SEI resistance (CPE_1) and contact resistance (R_f), the medium frequency semicircular can be explained as the charge-transfer impedance (R_{ct}) of the electrode reaction coupled with CPE_2 of the electrode/electrolyte interface, while the low-frequency sloping straight line corresponds to the Warburg impedance (Z_w), relating to solid-state diffusion of lithium ions in the bulk electrode (R_e).[36,53,64,65] As can be seen in Figure 4f and Figure S11a, it is quite obvious that the diameter of the semicircle for 3D FL-MoS_2@PCNN electrode before cycling or after the rate capability test at the high−medium frequency region is dramatically smaller than that of MoS_2/C composites and MoS_2 powders, suggesting that this unique 3D architecture can remarkably enhance the electrical conductivity and electrochemical reaction kinetics of the whole electrode. In addition, the kinetic parameters (R_f and R_{ct}) can be obtained by modeling AC impendence spectra on the basis of the modified Randles equivalent circuit (Figure S11b), with the fitted kinetic parameters exhibited in Table S2. As can be seen, the SEI film resistance R_f and charge-transfer resistance R_{ct} of the 3D FL-MoS_2@PCNN electrode after rate capability test are much lower than those of the MoS_2/C composite and MoS_2 powder electrodes after rate capability test, which validates that the 3D carbon nanosheet network and the intimate interfacial contact between MoS_2 and carbon nanosheets could effectively lower the contact resistance and charge transfer resistance of the composite electrode and thus give rise to enhanced electron transfer speed especially during the high-rate lithium insertion/extraction process, leading to much better rate performance of 3D FL-MoS_2@PCNNs than MoS_2/C composites and MoS_2 powders.

The above evidence clearly substantiates that our 3D FL-MoS_2@PCNN anode possesses high reversible capacity, excellent Coulombic efficiency, and superb long-life cycling capability at high rates, which should be associated with its unique microstructure that offers the following advantages. First, the highly flexible ultrathin carbon nanosheets that tightly anchor the 2D MoS_2 nanosheets can enable synchronous deformation along with volume change of MoS_2 nanosheets and thus can effectively prevent the peel off of MoS_2 nanosheets from the conductive carbon matrix during cycling. More importantly, the well-crystallized MoS_2 nanosheets coupled with intimate interfacial contact between the surfaces of MoS_2 and high-conducting carbon nanosheets can ensure fast and stable transport of both electrons and ions across the interface especially at high-rate charge/discharge cycling process, contributing to evidently enhanced high-rate cycling capacity and stability. Second, the 3D carbon nanosheet architecture with integrative nature, large surface area, and superior continuous conductive network can remarkably facilitate three-dimensional fast and efficient transport of both electrons and ions into the deep locations of the overall electrode.[37,42,53] Furthermore, their abundant macropores and mesopores can further provide sufficient void space for expansion of MoS_2 upon lithiation and hence mitigates the mechanical failure of the active materials after repeated lithiation/delithiation. Third, the ultrathin 2D nature of MoS_2 and carbon nanosheets can offer a mass of active sites for hosting lithium ions, and also can greatly shorten the diffusion distance of both electrons and ions, which is favorable for enhancing the high-rate cycling capacity and good Coulombic efficiency.[37,38,42,53] All of these points are responsible for the superior high-rate cycle performance of the 3D FL-MoS_2@PCNNs. In addition, the microstructure of the FL-MoS_2@PCNN electrode after long-term high-rate cyclability test has also been explored by TEM, STEM and elemental mapping. As shown in Figure S12, although the FL-MoS_2@PCNN electrode was cycled for over 520 cycles at 2 A g^{-1}, it still retains a homogeneous distribution of C, Mo, and S elements in the carbon nanosheets, further validating the fine high-rate cycling stability of this novel architecture.

CONCLUSIONS

In summary, we have developed a novel and scalable 2D space-confined strategy for the synthesis of few-layer MoS_2 nanosheets anchored on 3D porous carbon nanosheet networks as a high-performance LIB anode. 3D NaCl self-assembly was introduced to serve as a template to direct the growth of 3D porous carbon nanosheet networks and also offer a 2D-confined space for the *in situ* construction of few-layer MoS_2 nanosheets robustly lain on the surface of carbon nanosheet walls. In the built 3D architecture, the intimate surface-to-surface contact can effectively avoid the aggregation of MoS_2 nanosheets and remarkably enhance the structural stability of the electrode, while the 3D porous carbon nanosheet networks can enable fast transport of both electrons and ions in the overall electrode. As a consequence, this 3D architecture manifests an outstanding long-life cycling performance at high rates; it can deliver a specific capacity as large as 676 mAh g^{-1} even after 520 deep charge/discharge cycles at 2 A g^{-1} while showing a capacity retention as high as 95.2%. Apart from promising LIB anodes, it is believed that this 3D FL-MoS_2@PCNN hybrid also has immense potential for applications in other areas such as supercapacitor, catalysis, and sensors. Furthermore, this unique 2D space-confined synthesis protocol may be very suitable for scalable and low-cost industrial production of MoS_2/carbon composites and also can be easily

extended to the construction of other 2D nanostructures (such as metal sulfide/oxide) anchored on carbon nanosheet networks with an intimate interfacial contact for different applications.

METHODS

Preparation of 3D FL-MoS_2@PCNNs. In a typical synthesis of 3D FL-MoS_2@PCNNs, 1.401 g of citric acid, 0.3532 g of $(NH_4)_6Mo_7O_{24}\cdot 4H_2O$, 0.3654 g of CH_4N_2S and 17.55 g of NaCl were first dissolved in 100 mL of deionized water by magnetic stirring. The as-obtained homogeneous solution was then frozen in a refrigerator at −20 °C for 24 h. Subsequently, the water in the resulting gel is removed by freeze-drying and the obtained dry gel was ground to fine composite powder, which was then subjected to heat-treatment. During the heat-treatment process, the composite powder (∼10 g) was placed in a quartz boat located in the middle of the furnace tube and heated at 750 °C for 2 h under Ar. After that, the furnace tube was cooled down to room temperature in the presence of Ar. Finally, the NaCl in the as-made products were removed by deionized water to obtain pure 3D FL-MoS_2@PCNNs. For comparison, amorphous carbon blocks with MoS_2 embedded (MoS_2/C composite) were prepared by heat-treating the mixture of $(NH_4)_6Mo_7O_{24}\cdot 4H_2O$, CH_4N_2S and citric acid without adding NaCl at the same preparation conditions of 3D FL-MoS_2@PCNNs, MoS_2 nanosheets were obtained by calcining the mixture ($(NH_4)_6Mo_7O_{24}$/NaCl) without $C_6H_8O_7$ and NH_2CSNH_2 and its reaction product with H_2S, and 3D PCNNs were synthesized by heat-treating the mixture of $C_6H_8O_7$/NaCl without adding NH_2CSNH_2−$(NH_4)_6Mo_7O_{24}$.

Characterizations. XRD measurements were conducted on a Rigaku D/max 2500 diffractometer using Cu Kα radiation at a wavelength of 1.5406 Å. SEM was performed with a JSM-6700F scanning electron microscope. TEM, HRTEM, STEM and elemental mapping were carried out using a FEI Tecnai G^2 F20 field emission transmission electron microscope operated at 200 kV. EDX analysis was conducted on an EDAX system attached to the FEI Tecnai G^2 F20 microscope. TG analysis was performed with a PerkinElmer (TA Instruments) up to 700 °C at a heating rate of 10 °C/min in air. Raman spectrum was recorded on the LabRAM HR Raman spectrometer using laser excitation at 514.5 nm from an Ar ion laser source. XPS analysis was performed on an ESCALab220i-XL electron spectrometer from VG Scientific using 300 W Al Kα radiation. Nitrogen adsorption and desorption isotherms at 77.3 K were carried out with a ASAP 2020 physisorption analyzer (USA).

Electrochemical Measurements. The electrochemical properties of 3D FL-MoS_2@PCNNs, MoS_2/C composite, MoS_2 nanosheets, 3D PCNNs or commercial MoS_2 powders purchased from DK nanotechnology Co., Ltd., Beijing, were carried out using coin-type half-cell (CR2032). During the preparation of working electrodes, active materials, Super-P carbon black, and polyvinylidene fluoride (PVDF) with mass ratio 80:10:10 were mixed into a homogeneous slurry with mortar and pestle, and then the obtained slurry was pasted onto pure Cu foil. Lithium metal foil works as both counter and reference electrode, the electrolyte was $LiPF_6$ (1 M) in ethylene carbonate/dimethyl carbonate/diethyl carbonate (1:1:1 vol %). The tested cells were assembled in an argon-filled glovebox. CV was carried out on a CHI660D electrochemical workstation at a scan rate of 0.1 mV s^{-1} within the potential range of 0.005−3.0 V *vs* Li^+/Li. The discharge and charge measurements of the batteries were performed on a LAND CT2001A electrochemical workstation between 3.00 and 0.005 V at room temperature. Here the total weight of the active materials (3D FL-MoS_2@PCNNs, commercial MoS_2 powders, MoS_2/C composite, MoS_2 nanosheets or 3D PCNNs) was utilized to calculate the capacity values. Electrochemical impedance spectroscopy measurements were recorded on a CHI660D electrochemical workstation in the frequency range 100 kHz to 10 mHz.

Conflict of Interest: The authors declare no competing financial interest.

Acknowledgment. The authors acknowledge the financial support by the National Natural Science Foundation of China (No. 51422104, and No. 51472177) and Foundation for the Author of National Excellent Doctoral Dissertation of China (No. 201145), Program for New Century Excellent Talents in University (NCET-12-0408), and National Basic Research Program of China (2010CB934700).

Supporting Information Available: Supplementary SEM, TEM, EDS, XPS and BET analyses. This material is available free of charge *via* the Internet at http://pubs.acs.org.

REFERENCES AND NOTES

1. Kang, B.; Ceder, G. Battery Materials for Ultrafast Charging and Discharging. *Nature* **2009**, *458*, 190–193.
2. Cheng, F. Y.; Liang, J.; Tao, Z. L.; Chen, J. Functional Materials for Rechargeable Batteries. *Adv. Mater.* **2011**, *23*, 1695–1715.
3. Huang, X.; Zeng, Z. Y.; Zhang, H. Metal Dichalcogenide Nanosheets: Preparation, Properties and Applications. *Chem. Soc. Rev.* **2013**, *42*, 1934–1946.
4. Tan, C. L.; Zhang, H. Two-Dimensional Transition Metal Dichalcogenide Nanosheet-Based Composites. *Chem. Soc. Rev.* **2015**, 10.1039/c4cs00182f.
5. Hu, Zhe; Wang, L. X.; Zhang, K.; Wang, J. B.; Cheng, F. Y.; Tao, Z. L.; Chen, J. MoS_2 Nanoflowers with Expanded Interlayers as High-Performance Anodes for Sodium-Ion Batteries. *Angew. Chem., Int. Ed.* **2014**, *53*, 12794–12798.
6. Hong, X.; Liu, J. Q.; Zheng, B.; Huang, X.; Zhang, X.; Tan, C. L.; Chen, J. Z.; Fan, Z. X.; Zhang, H. A Universal Method for Preparation of Noble Metal Nanoparticle-Decorated Transition Metal Dichalcogenide Nanobelts. *Adv. Mater.* **2014**, *26*, 6250–6254.
7. Chang, K.; Geng, D.; Li, X.; Yang, J.; Tang, Y.; Cai, M.; Li, R.; Sun, X. Ultrathin MoS_2/Nitrogen-Doped Graphene Nanosheets with Highly Reversible Lithium Storage. *Adv. Energy Mater.* **2013**, *3*, 839–844.
8. Wang, P. P.; Sun, H.; Ji, Y.; Li, W.; Wang, X. Three-Dimensional Assembly of Single-Layered MoS_2. *Adv. Mater.* **2014**, *26*, 964–969.
9. Liu, H.; Su, D. W.; Zhou, R. F.; Sun, B.; Wang, G. X.; Qiao, S. Z. Highly Ordered Mesoporous MoS_2 with Expanded Spacing of the (002) Crystal Plane for Ultrafast Lithium Ion Storage. *Adv. Energy Mater.* **2012**, *2*, 970–975.
10. Hwang, H.; Kim, H.; Cho, J. MoS_2 Nanoplates Consisting of Disordered Graphene-Like Layers for High Rate Lithium Battery Anode Materials. *Nano Lett.* **2011**, *11*, 4826–4830.
11. Zhang, L.; Wu, H. B.; Yan, Y.; Wang, X.; (David) Lou, X. W. Hierarchical MoS_2 Microboxes Constructed by Nanosheets with Enhanced Electrochemical Properties for Lithium Storage and Water Splitting. *Energy Environ. Sci.* **2014**, *7*, 3302–3306.
12. Yang, T.; Chen, Y. J.; Qu, B. H.; Mei, L.; Lei, D. N.; Zhang, H. N.; Li, Q. H.; Wang, T. H. Construction of 3D Flower-Like MoS_2 Spheres with Nanosheets as Anode Materials for High-Performance Lithium Ion Batteries. *Electrochim. Acta* **2014**, *115*, 165–169.
13. Liu, Y. D.; Ren, L.; Qi, X.; Yang, L. W.; Li, J.; Wang, Y.; Zhong, J. X. Hydrothermal Exfoliated Molybdenum Disulfide Nanosheets as Anode Material for Lithium Ion Batteries. *J. Energy Chem.* **2014**, *23*, 207–212.
14. Wang, S. Q.; Li, G. H.; Du, G. D.; Jiang, X. Y.; Feng, C. Q.; Guo, Z. P.; Kim, S. J. Hydrothermal Synthesis of Molybdenum Disulfide for Lithium Ion Battery Applications. *Chin. J. Chem. Eng.* **2010**, *18*, 910–913.
15. Fang, X. P.; Yu, X. Q.; Liao, S. F.; Shi, Y. F.; Hu, Y. S.; Wang, Z. X.; Stucky, G. D.; Chen, L. Q. Lithium Storage Performance in

Ordered Mesoporous MoS_2 Electrode Material. *Microporous Mesoporous Mater.* **2012**, *151*, 418–423.
16. Wang, X. W.; Zhang, Z.; Chen, Y. Q.; Qu, Y. H.; Lai, Y. Q.; Li, J. Morphology-Controlled Synthesis of MoS_2 Nanostructures with Different Lithium Storage Properties. *J. Alloys Compd.* **2014**, *600*, 84–90.
17. Feng, C. Q.; Ma, J.; Li, H.; Zeng, R.; Guo, Z. P.; Liu, H. K. Synthesis of Molybdenum Disulfide (MoS_2) for Lithium Ion Battery Applications. *Mater. Res. Bull.* **2009**, *44*, 1811–1815.
18. Wang, M.; Li, G. D.; Xu, H. Y.; Qian, Y. T.; Yang, J. Enhanced Lithium Storage Performances of Hierarchical Hollow MoS_2 Nanoparticles Assembled from Nanosheets. *ACS Appl. Mater. Interfaces* **2013**, *5*, 1003–1008.
19. Ding, S. J.; Zhang, D. Y.; Chen, J. S.; Lou, X. W. (David) Facile Synthesis of Hierarchical MoS_2 Microspheres Composed of Few-Layered Nanosheets and Their Lithium Storage Properties. *Nanoscale* **2012**, *4*, 95–98.
20. Yang, L. C.; Wang, S. N.; Mao, J. J.; Deng, J. W.; Gao, Q. S.; Tang, Y.; Schmidt, O. G. Hierarchical MoS_2/Polyaniline Nanowires with Excellent Electrochemical Performance for Lithium-Ion Batteries. *Adv. Mater.* **2013**, *25*, 1180–1184.
21. Xu, X.; Fan, Z. Y.; Yu, X. Y.; Ding, S. J.; Yu, D. M.; (David) Lou, X. W. A Nanosheets-on-Channel Architecture Constructed from MoS_2 and CMK-3 for High-Capacity and Long-Cycle-Life Lithium Storage. *Adv. Energy Mater.* **2014**, 1400902.
22. Zhang, C. F.; Wu, H. B.; Guo, Z. P.; Lou, X. W. Facile Synthesis of Carbon-Coated MoS_2 Nanorods with Enhanced Lithium Storage Properties. *Electrochem. Commun.* **2012**, *20*, 7–10.
23. Zhao, C. Y.; Kong, J. H.; Yao, X. Y.; Tang, X. S.; Dong, Y. L.; Phua, S. L.; Lu, X. H. Thin MoS_2 Nanoflakes Encapsulated in Carbon Nanofibers as High-Performance Anodes for Lithium-Ion Batteries. *ACS Appl. Mater. Interfaces* **2014**, *6*, 6392–6398.
24. Zhou, F.; Xin, S.; Liang, H. W.; Song, L. T.; Yu, S. H. Carbon Nanofibers Decorated with Molybdenum Disulfide Nanosheets: Synergistic Lithium Storage and Enhanced Electrochemical Performance. *Angew. Chem., Int. Ed.* **2014**, *53*, 11552–11556.
25. Qiu, W. D.; Xia, J.; He, S. X.; Xu, H. J.; Zhong, H. M.; Chen, L. P. Facile Synthesis of Hollow MoS_2 Microspheres/Amorphous Carbon Composites and Their Lithium Storage Properties. *Electrochim. Acta* **2014**, *117*, 145–152.
26. Zhang, L.; Lou, X. W. Hierarchical MoS_2 Shells Supported on Carbon Spheres for Highly Reversible Lithium Storage. *Chem.—Eur. J.* **2014**, *20*, 5219–5223.
27. Zhou, X. S.; Wan, L. J.; Guo, Y. G. Facile Synthesis of MoS_2@CMK-3 Nanocomposite as an Improved Anode Material for Lithium-Ion Batteries. *Nanoscale* **2012**, *4*, 5868–5871.
28. Wang, Y.; Xing, G. Z.; Han, Z. J.; Shi, Y. M.; Wong, J. I.; Huang, Z. X.; Ostrikovcde, K.; Yang, H. Y. Pre-Lithiation of Onion-Like Carbon/MoS_2 Nanourchin Anodes for High-Performance Rechargeable Lithium Ion Batteries. *Nanoscale* **2014**, *6*, 8884–8890.
29. Das, S. K.; Mallavajula, R.; Jayaprakash, N.; Archer, L. A. Self-Assembled MoS_2—Carbon Nanostructures: Influence of Nanostructuring and Carbon on Lithium Battery Performance. *J. Mater. Chem.* **2012**, *22*, 12988–12992.
30. Chang, K.; Chen, W. X.; Ma, L.; Li, H.; Li, H.; Huang, F. H.; Xu, Z. D.; Zhang, Q. B.; Lee, J. Y. Graphene-Like MoS_2/Amorphous Carbon Composites with High Capacity and Excellent Stability as Anode Materials for Lithium Ion Batteries. *J. Mater. Chem.* **2011**, *21*, 6251–6257.
31. Wang, J. Z.; Lu, L.; Lotya, M.; Coleman, J. N.; Chou, S. L.; Liu, H. K.; Minett, A. I.; Chen, J. Development of MoS_2—CNT Composite Thin Film from Layered MoS_2 for Lithium Batteries. *Adv. Energy Mater.* **2013**, *3*, 798–805.
32. Gao, P. Y.; Yangn, Z. X.; Liu, G. M.; Qiao, Q. D. Facile Synthesis of MoS_2/MWNT Anode Material for High-Performance Lithium-Ion Batteries. *Ceram. Int.* **2015**, *41*, 1921–1925.
33. Shi, Y. M.; Wang, Y.; Wong, J. I.; Tan, A. Y. S.; Hsu, C. L.; Li, L. J.; Lu, Y. C.; Yang, H. Y. Self-Assembly of Hierarchical MoS_x/CNT Nanocomposites ($2 < x < 3$): towards High Performance Anode Materials for Lithium Ion Batteries. *Sci. Rep.* **2013**, *3*, 2169.
34. Ding, S. J.; Chen, J. S.; Lou, X. W. Glucose-Assisted Growth of MoS_2 Nanosheets on CNT Backbone for Improved Lithium Storage Properties. *Chem.—Eur. J.* **2011**, *17*, 13142–13145.
35. Lu, C. X.; Liu, W. W.; Li, H.; Tay, B. K. A Binder-Free CNT Network—MoS_2 Composite as a High Performance Anode Material in Lithium Ion Batteries. *Chem. Commun.* **2014**, *50*, 3338–3340.
36. Ma, L.; Ye, J. B.; Chen, W. X.; Chen, D. Y.; Lee, J. Y. Gemini Surfactant Assisted Hydrothermal Synthesis of Nanotile-Like MoS_2/Graphene Hybrid with Enhanced Lithium Storage Performance. *Nano Energy* **2014**, *10*, 144–152.
37. Cao, X. H.; Shi, Y. M.; Shi, W. H.; Rui, X. H.; Yan, Q. Y.; Kong, J.; Zhang, H. Preparation of MoS_2-Coated Three-Dimensional Graphene Networks for High-Performance Anode Material in Lithium-Ion Batteries. *Small* **2013**, *9*, 3433–3438.
38. Gong, Y. J.; Yang, S. B.; Zhan, L.; Ma, L. L.; Vajtai, R.; Ajayan, P. M. A Bottom-Up Approach to Build 3D Architectures from Nanosheets for Superior Lithium Storage. *Adv. Funct. Mater.* **2014**, *24*, 125–130.
39. Fu, W.; Du, F. H.; Su, J.; Li, X. H.; Wei, X.; Ye, T. N.; Wang, K. X.; Chen, J. S. *In Situ* Catalytic Growth of Large-Area Multilayered Graphene/MoS_2 Heterostructures. *Sci. Rep.* **2014**, *4*, 4673.
40. Yu, H. L.; Ma, C.; Ge, B. H.; Chen, Y. J.; Xu, Z.; Zhu, C. L.; Li, C. Y.; Ouyang, Q. Y.; Gao, P.; Li, J. Q.; *et al.* Three-Dimensional Hierarchical Architectures Constructed by Graphene/MoS_2 Nanoflake Arrays and Their Rapid Charging/Discharging Properties as Lithium-Ion Battery Anodes. *Chem.—Eur. J.* **2013**, *19*, 5818–5823.
41. Chang, K.; Chen, W. L-Cysteine-Assisted Synthesis of Layered MoS_2/Graphene Composites with Excellent Electrochemical Performances for Lithium Ion Batteries. *ACS Nano* **2011**, *5*, 4720–4728.
42. Wang, J.; Liu, J. L.; Chao, D. L.; Yan, J. X.; Lin, J. Y.; Shen, Z. X. Self-Assembly of Honeycomb-Like MoS_2 Nanoarchitectures Anchored into Graphene Foam for Enhanced Lithium-Ion Storage. *Adv. Mater.* **2014**, *26*, 7162–7169.
43. Liu, Y. C.; Zhao, Y. P.; Jiao, L. F.; Chen, J. A Graphene-Like MoS_2/Graphene Nanocomposite as a High Performance Anode for Lithium Ion Batteries. *J. Mater. Chem. A* **2014**, *2*, 13109–13115.
44. Guo, J.; Chen, X.; Jin, S. H.; Zhang, M. M.; Liang, C. H. Synthesis of Graphene-Like MoS_2 Nanowall/Graphene Nanosheet Hybrid Materials with High Lithium Storage Performance. *Catal. Today* **2015**, *246*, 165–171.
45. Han, S.; Zhao, Y. R.; Tang, Y. P.; Tan, F. Z.; Huang, Y. S.; Feng, X. L.; Wu, D. Q. Ternary MoS_2/SiO_2/Graphene Hybrids for High-Performance Lithium Storage. *Carbon* **2015**, *81*, 203–209.
46. Yu, J.; Edwin, O. O.; Carlos, R. C.; Chen, Z. F.; Zhou, Z. Layer-by-Layer Hybrids of MoS_2 and Reduced Graphene Oxide for Lithium Ion Batteries. *Electrochim. Acta* **2014**, *147*, 392–400.
47. Hou, Y.; Li, J. Y.; Wen, Z. H.; Cui, S. M.; Yuan, C.; Chen, J. H. N-Doped Graphene/Porous g-C_3N_4 Nanosheets Supported Layered-MoS_2 Hybrid as Robust Anode Materials for Lithium-Ion Batteries. *Nano Energy* **2014**, *8*, 157–164.
48. Pham, V. H.; Kim, K. H.; Jung, D. W.; Singh, K.; Oh, E. S.; Chung, J. S. Liquid Phase Co-Exfoliated MoS_2—Graphene Composites as Anode Materials for Lithium Ion Batteries. *J. Power Sources* **2013**, *244*, 280–286.
49. Liu, G.; Feng, Y. Y.; Li, Y.; Qin, M. M.; An, H. R.; Hu, W. P.; Feng, W. Three-Dimensional Multilayer Assemblies of MoS_2/Reduced Graphene Oxide for High-Performance Lithium Ion Batteries. *Part. Part. Syst. Charact.* **2014**, 10.1002/ppsc.201400207.
50. Ma, L.; Huang, G. C.; Chen, W. X.; Wang, Z.; Ye, J. B.; Li, H. Y.; Chen, D. Y.; Lee, J. Y. Cationic Surfactant-Assisted Hydrothermal Synthesis of Few-Layer Molybdenum Disulfide/Graphene Composites: Microstructure and Electrochemical Lithium Storage. *J. Power Sources* **2014**, *264*, 262–271.
51. Nandi, D. K.; Uttam, K. S.; Choudhury, D.; Mitra, S.; Sarkar, S. K. Atomic Layer Deposited MoS_2 as a Carbon and Binder Free Anode in Li-Ion Battery. *Electrochim. Acta* **2014**, *146*, 706–713.

52. Wang, Z.; Chen, T.; Chen, W. X.; Chang, K.; Ma, L.; Huang, G. C.; Chen, D. Y.; Lee, J. Y. CTAB-Assisted Synthesis of Single-Layer MoS_2−Graphene Composites as Anode Materials of Li-Ion Batteries. *J. Mater. Chem. A* **2013**, *1*, 2202–2210.
53. Qin, J.; He, C. N.; Zhao, N. Q.; Wang, Z. Y.; Shi, C. S.; Liu, E. Z.; Li, J. J. Graphene Networks Anchored with Sn@Graphene as Lithium Ion Battery Anode. *ACS Nano* **2014**, *8*, 1728–1738.
54. Luo, B.; Wang, B.; Li, X. L.; Jia, Y. Y.; Liang, M. H.; Zhi, L. J. Graphene-Confined Sn Nanosheets with Enhanced Lithium Storage Capability. *Adv. Mater.* **2012**, *24*, 3538–3543.
55. Zhou, G. M.; Wang, D. W.; Yin, L. C.; Li, N.; Li, F.; Cheng, H. M. Oxygen Bridges between NiO Nanosheets and Graphene for Improvement of Lithium Storage. *ACS Nano* **2012**, *6*, 3214–3223.
56. Wu, Z. S.; Ren, W. C.; Wen, L.; Gao, L. B.; Zhao, J. P.; Chen, Z. P.; Zhou, G. M.; Li, F.; Cheng, H. M. Graphene Anchored with Co_3O_4 Nanoparticles as Anode of Lithium Ion Batteries with Enhanced Reversible Capacity and Cyclic Performance. *ACS Nano* **2010**, *4*, 3187–3194.
57. Roy, K.; Padmanabhan, M.; Goswami, S.; Sai, T. P.; Ramalingam, G.; Raghavan, S.; Ghosh, A. Graphene-MoS_2 Hybrid Structures for Multifunctional Photoresponsive Memory Devices. *Nat. Nanotechnol.* **2013**, *8*, 826–830.
58. Hong, X. P.; Kim, J.; Shi, S. F.; Zhang, Y.; Jin, C. H.; Sun, Y. H.; Tongay, S.; Wu, J. Q.; Zhang, Y. F.; Wang, F. Ultrafast Charge Transfer in Atomically Thin MoS_2/WS_2 Heterostructures. *Nat. Nanotechnol.* **2014**, *9*, 682–686.
59. Zhang, J.; Yu, H.; Chen, W.; Tian, X. Z.; Liu, D. H.; Cheng, M.; Xie, G. B.; Yang, W.; Yang, R.; Bai, X. D.; *et al.* Scalable Growth of High-Quality Polycrystalline MoS_2 Monolayers on SiO_2 with Tunable Grain Sizes. *ACS Nano* **2014**, *8*, 6024–6030.
60. Liu, Y. N.; Ghosh, R.; Wu, D.; Ismach, A.; Ruoff, R.; Lai, K. J. Mesoscale Imperfections in MoS_2 Atomic Layers Grown by a Vapor Transport Technique. *Nano Lett.* **2014**, *14*, 4682–4686.
61. Wang, X. S.; Feng, H. B.; Wu, Y. M.; Jiao, L. Y. Controlled Synthesis of Highly Crystalline MoS_2 Flakes by Chemical Vapor Deposition. *J. Am. Chem. Soc.* **2013**, *135*, 5304–5307.
62. Song, I.; Park, C.; Hong, M.; Baik, J.; Shin, H. J.; Choi, H. C. Patternable Large-Scale Molybdenium Disulfide Atomic Layers Grown by Gold-Assisted Chemical Vapor Deposition. *Angew. Chem., Int. Ed.* **2014**, *126*, 1290–1293.
63. Sevilla, M.; Fuertes, A. B. Direct Synthesis of Highly Porous Interconnected Carbon Nanosheets and Their Application as High-Performance Supercapacitors. *ACS Nano* **2014**, *8*, 5069–5078.
64. He, C.; Wu, S.; Zhao, N.; Shi, C.; Liu, E.; Li, J. Carbon-Encapsulated Fe_3O_4 Nanoparticles as a High-Rate Lithium Ion Battery Anode Material. *ACS Nano* **2013**, *7*, 4459–4469.
65. Ji, H. X.; Zhang, L. L.; Pettes, M. T.; Li, H. F.; Chen, S. S.; Shi, L.; Piner, R.; Ruoff, R. S. Ultrathin Graphite Foam: A Three-Dimensional Conductive Network for Battery Electrodes. *Nano Lett.* **2012**, *12*, 2446–2451.